Optics Letters

Virtual X-ray critical dimension metrology via Monte Carlo simulation

Jiahao Zhang,[1,†] Zhangyong Liu,[1,†] Weigang Zhou,[1] Dingxuan Deng,[1] Xiuguo Chen,[1,2,*] and Shiyuan Liu[1,2]

[1]State Key Laboratory of Intelligent Manufacturing Equipment and Technology, Huazhong University of Science and Technology, Wuhan 430074, China
[2]Optics Valley Laboratory, Wuhan 430074, China
[†]These authors contributed equally to this work.
*xiuguochen@hust.edu.cn

Received 15 July 2024; revised 8 October 2024; accepted 18 October 2024; posted 22 October 2024; published 15 November 2024

X-ray critical dimension (XCD) metrology is a highly promising technique for achieving sub-nanometer precision in critical dimension measurements at advanced nodes of integrated circuit manufacturing. Compared to XCD experiments utilizing synchrotron radiation sources, those employing compact X-ray sources encounter challenges like extended testing time and increased uncertainty. To evaluate the influence of experimental conditions on measurement results, we developed an *ab initio* virtual X-ray critical dimension metrology via a Monte Carlo simulation (MC-VXCD). Through calibrating the system parameters of the MC-VXCD to a home-built compact XCD instrument, we achieved excellent consistency between virtual and actual measurement results. The virtual instrument effectively estimated measurement errors stemming from the reduced exposure time, which significantly influences the measurement accuracy and throughput. Furthermore, through the MC-VXCD, we establish the connection between the application scenarios of the XCD metrology and the geometry of XCD instruments, offering a versatile platform for the system design, experimental configuration optimization, data analysis, etc., in XCD metrology.

https://doi.org/10.1364/OL.536611

X-ray critical dimension (XCD) metrology, leveraging the high sensitivity of X-ray to electron density distribution in nanostructures, is emerging as an advanced nanostructure metrology for integrated circuit production lines [1–3]. The synchrotron radiation-based XCD metrology has achieved high-precision nanostructure measurements [4,5]. In production line applications, XCD measurements using compact sources are currently applied to high aspect ratio memory devices, benefiting from the signal enhancement due to the increased scattering volume [6–8]. Although the development of high-brightness desktop X-ray sources has significantly advanced the application of XCD metrology [9], fully utilizing the source flux and accurately estimating the exposure time still remain critical for improving measurement accuracy and reducing uncertainty [10,11]. Addressing this issue necessitates the establishment of a simulation model for the XCD system, which will directly facilitate the selection of the XCD system hardware, configuration, and measurement protocols.

Current XCD simulations primarily focus on the scattering process of X-ray interacting with nanostructure samples [12]. However, significant deficiencies remain in modeling the XCD instrument as a whole. While some studies have thoroughly examined the impact of factors such as X-ray beam divergence and spectral bandwidth on XCD measurement results [13], the propagation of X-ray within the entire instrument, such as the collimation system, is mainly modeled based on geometric relationships [14,15]. This approach fails to account for the response differences when different X-ray multilayer optics are used as inputs. Furthermore, the analysis of the system measurement noise and system configuration is still limited [16].

X-ray tracing based on the Monte Carlo (MC) method, which simulates the propagation of each photon within the system and its interactions with system components, has been widely adopted and highly regarded in the design of X-ray scattering systems and the simulation of scattering processes [17–20]. Simulation algorithms based on McXtrace software can estimate noise in scattering data and assess the impact of exposure time on the information content of the scattering data [21], demonstrating the capability of the MC method in X-ray system modeling. In XCD metrology, despite the significant costs associated with conducting experiments using either synchrotron radiation sources or compact small-angle X-ray scattering instruments, to the best of our knowledge, no virtual instrument has been established for such purposes. Given that XCD measurement demands exceptionally high-flux light sources and exhibits extreme sensitivity to experimental noise, a virtual instrument can offer valuable insights into the system design and data analysis, leading to significant savings in both time and financial resources.

In this Letter, we develop a virtual X-ray critical dimension metrology via the Monte Carlo method (MC-VXCD). Our main contributions are twofold. First, through calibrating the system parameters of the MC-VXCD to a home-built compact XCD instrument, we achieve excellent consistency between virtual and actual measurement results. MC-VXCD also reproduces the

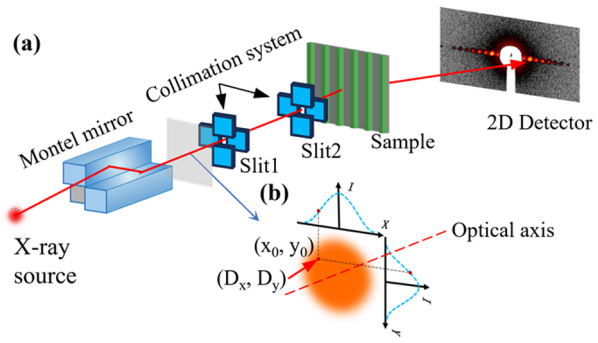

Fig. 1. (a) Schematic of the basic system layout for MC-VXCD. (b) Illustration of the photon sampling in the EM plane, where each photon's properties include its position (x_0, y_0), direction (D_x, D_y), and energy (E).

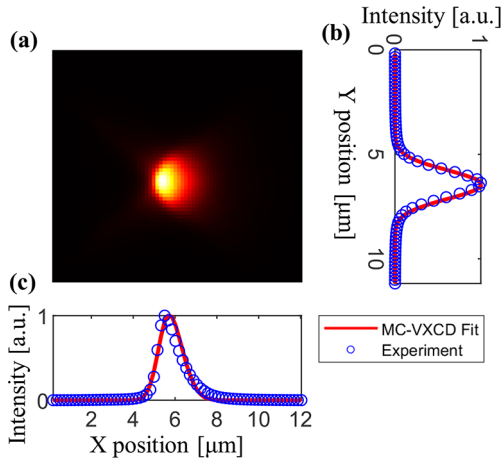

Fig. 2. System calibration results based on MC-VXCD. (a) Primary beam collected at a distance of 7250 mm between the detector and the EM plane. (b) and (c) Experimental and MC-VXCD fitted normalized intensity distribution curves by one-dimensional integration of the primary beam along the vertical and horizontal directions.

impact of measurement time on measurement error observed in real experiments, proving itself as a substitute for actual measurements. Second, we employ the MC-VXCD to analyze the influence of XCD system configurations on measurement results, demonstrating the method's significant role in guiding system construction and optimization, which will enhance the application prospects of XCD metrology and instruments in integrated circuit measurements.

Working principle. Figure 1 presents a schematic diagram of the MC-VXCD system. At the exit plane of the Montel mirror (EM plane), the beam, which has been monochromatized and collimated by the Montel mirror, is described as a collection of X-ray photons. As shown in Fig. 1(b), each photon's properties include its position (x_0, y_0), propagation direction (D_x, D_y), and energy (E). After passing through a collimation system consisting of two slits, the beam's diameter and divergence are further constrained. Subsequently, the photons interact with the nanostructure and are ultimately collected by a two-dimensional position sensitive detector, resulting in the scattering pattern of the sample within this measurement system.

The interaction between the nanostructure and X-ray photons involves absorption, transmission, and scattering, with scattering modeling being crucial for XCD simulations. According to the first-order Born approximation theory of X-ray scattering, the scattering intensity is the Fourier transform of the electron density distribution in the nanostructure. MC-VXCD first calculates the scattering cumulative distribution function (SCDF) composed of the intensities of various diffraction orders. For each photon, a uniformly distributed random number ε in the range of (0,1) is generated, and its interval ($SCDF_{m-1}$, $SCDF_m$) is determined, where m represents the m-th diffraction order. The scattering angle 2θ of the photon satisfies the Bragg equation [22]:

$$2\theta = \frac{m\lambda}{\text{pitch} \cdot \cos(\omega)}, \tag{1}$$

where λ is the photon wavelength, pitch is the period of the nanostructure, and ω is the measurement incident angle. A detailed description of the virtual instrument model is provided in Section 1 of Supplement 1.

Results and discussion. Our laboratory-scale XCD system utilizes a high-brightness liquid metal-jet X-ray source D2 from Excillum AB with a 70 kV high-voltage generator and maximum power of 250 W. The monochromatic X-ray beam emitted from the Montel mirror corresponds to the characteristic energy of In Kα at 24.1 keV. The collimation system incorporates two four-blade scatterless slits [23], and a Pilatus photon-counting detector with a CdTe sensor ensures high quantum efficiency and dark current-free data acquisition [24].

Accurate system calibration to our constructed system can be achieved to customize the virtual instrument and replicate it as a digital twin of the actual instrument. The system calibration process comprises two steps [25]. The first step involves calibrating the intensity distribution and divergence of the beam. With the slits fully open, the distance between the detector and the EM plane is varied to collect the primary beam. Figure 2(a) shows the primary beam image at a distance of 7250 mm between the detector and the EM plane. Beam parameter calibration is conducted based on the normalized one-dimensional integration curves of the primary beam in the horizontal and vertical directions. In MC-VXCD, the photon position and divergence are set to follow a Gaussian distribution [17]. Note that an asymmetric intensity distribution occurs in the horizontal direction and the divergence in that direction can be described by a skewed Gaussian distribution for more accurate fitting in this case, as shown in Figs. 2(b) and 2(c).

The second step, based on the previously calibrated beam parameters, involves calibrating the positions of the system components interacting with the beam, specifically the relative position of the slits to the beam center. Each slit edge is individually adjusted until complete extinction is achieved, resulting in a curve of the primary beam flux as a function of the positions of the eight slit edges. The relative position of each slit edge to the beam center in MC-VXCD is calibrated, thereby enabling precise control of the collimation system configuration. All measurements and calibration results from the entire process are detailed in Section 2 of Supplement 1.

Following the calibration of MC-VXCD to the home-built XCD system, certain simplifications can be applied to accelerate the simulation process while maintaining accuracy. Given the extremely weak scattering from nanostructures, with most photons either absorbed by the substrate or blocked by the beamstop after penetrating the substrate, it is feasible to disregard

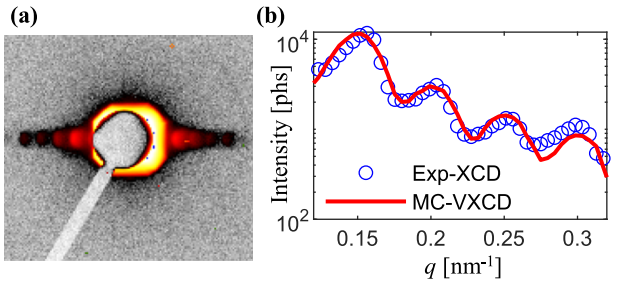

Fig. 3. (a) XCD scattering pattern of a one-dimensional nanostructure with 9000 s exposure time. (b) Comparison of one-dimensional integrated scattering intensity curves between the MC-VXCD and actual measurements under the same experimental configuration.

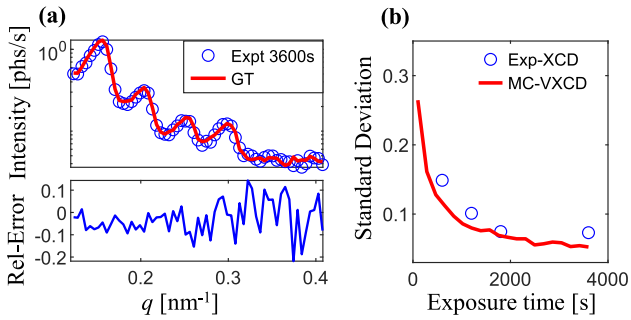

Fig. 4. (a) Relative error between the scattering curve and ground truth (GT) for an exposure time of 3600 s. (b) Standard deviation of scattering curves derived from MC-VXCD and experimental measurements as a function of exposure time.

these events and focus solely on the scattered photons. Using a one-dimensional trapezoidal cross section nanostructure, which was previously calibrated at the X-ray scattering beamline of the Shanghai Synchrotron Radiation Facility (see Section 1.2 in Supplement 1), we conducted measurements at normal incidence on the home-built XCD system. The experimental configuration included slit openings of $0.62 \times 0.62\,\mathrm{mm}^2$ and $0.56 \times 0.56\,\mathrm{mm}^2$ for Slit1 and Slit2, respectively, sample-detector distance (SDD) of 4267 mm, beamstop diameter of 6 mm, beam flux of 3.55×10^7 phs/s and exposure time of 9000 s. The measured scattering pattern is presented in Fig. 3(a). For comparison, the same measurement conditions were applied in MC-VXCD, and one-dimensional integrations of the actual and virtual scattering patterns were calculated, as depicted in Fig. 3(b). The two scattering curves versus q, where q is the magnitude of scattering vector with $q = 4\pi \sin\theta/\lambda$, demonstrated excellent consistency, validating the simulation capability of the proposed virtual instrument.

MC-VXCD enables the quantitative and precise estimation of the scattering signal error. For application to production lines, the XCD method must enhance the throughput by minimizing the measurement time without sacrificing accuracy. Due to the higher signal-to-noise ratio of the scattering signal from long exposure times, which reduces the impact of random noise, we selected the time-normalized scattering curve from a 9000 s exposure as the ground truth (GT). Then, we shortened the measurement times to 3600, 1800, 1200, and 600 s, without altering other experimental configurations of the home-built instrument. The relative errors of resulting time-normalized scattering curves compared to the GT were calculated [26]. Figure 4(a) presents the scattering curve for a 3600 s exposure and its relative error, showing greater error in the higher scattering vector, where the theoretical intensity is lower. The definition of relative errors for time-normalized scattering curves and results at other exposure times are detailed in Section 3 of Supplement 1. Similarly, we varied the exposure time in the MC-VXCD, and the standard deviations of the relative errors compared to the virtual scattering curve for a 9000 s exposure time were calculated. As shown in Fig. 4(b), for the relatively short exposure time, increasing the exposure time rapidly decreases the standard deviation. However, once the exposure time reaches a certain point, the decrease in standard deviation becomes more gradual and stabilizes, which is consistent with experimental results. While increasing the exposure time significantly improves the signal-to-noise ratio, excessively long exposure durations severely impact the measurement throughput. The

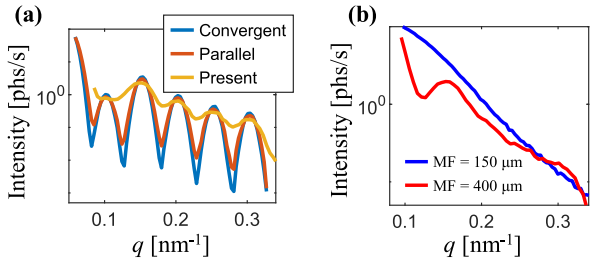

Fig. 5. (a) XCD scattering curves for different beam properties, with Convergent denoted the beam converging on the detection plane, Parallel denoted the ideally parallel beam, and Present denoted the beam of the home-built XCD instrument. (b) Scattering curves at different sizes of MF when the sample is located at the rear focus of the beam.

MC-VXCD shows the ability to offer a balanced evaluation of the throughput and signal quality.

The MC-VXCD not only replaces the actual measurement process but also provides guidance for selecting experimental devices and configurations. Compared to XCD experiments based on synchrotron radiation sources, compact XCD instruments typically exhibit larger divergence, resulting in more pronounced smearing effects. An alternative approach involves using convergent multilayer mirrors to focus the beam onto the detector surface [27]. We compared the scattering curves of nanostructures using the current beam, ideal parallel, and convergence on the detection surface, as illustrated in Fig. 5(a). Focusing the beam onto the detection surface effectively suppresses the smearing effects, thereby significantly improving the quality of the measurement data and reducing the uncertainty in extracting nanostructure parameters.

In production line measurements, however, the gratings used for detection are usually located in the scribe lines between the chips, which have very limited areas. When the beam converges on the detection surface, the larger spot size at the sample introduces scattering signals from non-detection areas, affecting the scattering measurement results. One solution is to use a micro-focus (MF) multilayer mirror, placing the sample at its rear focal point to ensure the beam only scatters in the detection grating area. As illustrated in Fig. 5(b), we generated scattering curves of nanostructures at MF of 400 and 150 μm, respectively. The converging beam directed at the sample will diverge after scattering. A smaller focal spot leads to larger divergence, causing a severe overlap of scattering peaks, which presents significant

challenges for data analysis. Fortunately, many desmearing algorithms have been developed for small-angle scattering, capable of recovering scattering peaks from highly smeared scattering curves [28]. Additionally, the virtual instrument's capability to rapidly generate large amounts of virtual scattering data holds significant potential for the integration with machine learning. It is promising to enhance the signal-to-noise ratio of scattering data and suppress smearing effects simultaneously by training neural networks [29].

Conclusion. Our proposal introduces a virtual X-ray critical dimension metrology via Monte Carlo simulation (MC-VXCD). Utilizing X-ray photon tracing, we develop a comprehensive model of the XCD system. After calibration to the home-built XCD system, the validity of the MC-VXCD is verified by its consistency with actual measurement results and accurate estimation of measurement errors caused by exposure time. It is important to note that the sources of the background noise are complex, including cosmic background radiation, parasitic scattering introduced by various experimental devices and so on. Our future work will provide a more detailed analysis of these noise sources and utilize the virtual instrument to provide significant guidance for improving the geometric design of actual instruments and data analysis algorithms. The lab-scale XCD instrument is currently applied in the inspection of memory devices. Leveraging the insights from the virtual instrument, XCD metrology is expected to be further utilized in the inspection of logic chips with complex integrated 3D architectures [2].

Funding. National Natural Science Foundation of China (52022034, 62175075, 52130504).

Disclosures. The authors declare no conflicts of interest.

Data availability. Data underlying the results presented in this paper are not publicly available at this time but may be obtained from the authors upon reasonable request. The MC-VXCD codes are available from the authors upon reasonable request.

Supplemental document. See Supplement 1 for supporting content.

REFERENCES

1. "International roadmap for devices and systems (IRDS), metrology (Table MET-3)" (2022), https://irds.ieee.org.
2. W. L. Wu, R. J. Kline, R. L. Jones, *et al.*, J. Micro/Nanopattern. Mats. Metro. **22**, 031206 (2023).
3. N. G. Orji, M. Badaroglu, B. M. Barnes, *et al.*, Nat. Electron. **1**, 532 (2018).
4. D. F. Sunday, S. List, J. S. Chawla, *et al.*, J. Appl. Crystallogr. **48**, 1355 (2015).
5. J. Reche, P. Gergaud, Y. Blancquaert, *et al.*, IEEE Trans. Semicond. Manufact. **35**, 425 (2022).
6. W. E. Fu, B. C. He, and W. L. Wu, Surf. Topogr.: Metrol. Prop. **11**, 024008 (2023).
7. R. Suenaga, Y. Ito, T. Goto, *et al.*, J. Appl. Phys. **62**, 096502 (2023).
8. T. G. Dziura, A. A. Gellineau, and A. V. Shchegrov, "X-ray scatterometry metrology for high aspect ratio structures," U.S. patent 10,352,695B2 (15 June 2017).
9. M. Wansleben, C. Zech, C. Streeck, *et al.*, J. Anal. At. Spectrom. **34**, 1497 (2019).
10. D. F. Sunday and R. J. Kline, J. Micro/Nanolithogr., MEMS, MOEMS **17**, 1 (2018).
11. D. F. Sunday, S. List, J. S. Chawla, *et al.*, J. Micro/Nanolith. MEMS MOEMS **15**, 014001 (2016).
12. D. Wang, H. Liang, H. Yang, *et al.*, J. Appl. Phys. **135**, 223103 (2024).
13. Z. Ma and D. G. Seiler, *Metrology and Diagnostic Techniques for Nanoelectronics* (Pan Stanford Publishing, 2016), Chap. 2.
14. Z. Li, D. Li, Z. Wu, *et al.*, J. X-ray Sci. Technol. **20**, 331 (2012).
15. A. Wacha, J. Appl. Crystallogr. **48**, 1843 (2015).
16. S. M. Sedlak, L. K. Bruetzel, and J. Lipfert, J. Appl. Crystallogr. **50**, 621 (2017).
17. E. B. Knudsen, A. Prodi, J. Baltser, *et al.*, J. Appl. Crystallogr. **46**, 679 (2013).
18. L. Rebuffi and M. S. Rio, J. Synchrotron Radiat. **23**, 1357 (2016).
19. M. Sanchez del Rio, R. Celestre, M. Glass, *et al.*, J. Synchrotron Radiat. **26**, 1887 (2019).
20. J. C. E. A. Hafner, T. Kluyver, M. Bertelsen, *et al.*, Proc. SPIE **11493**, 114930Z (2020).
21. A. H. Larsen and M. C. Pedersen, J. Appl. Crystallogr. **54**, 1281 (2021).
22. J. Wernecke, F. Scholze, and M. Krumrey, Rev. Sci. Instrum. **83**, 103906 (2012).
23. Y. Li, R. Beck, T. Huang, *et al.*, J. Appl. Crystallogr. **41**, 1134 (2008).
24. J. Wernecke, C. Gollwitzer, P. Müller, *et al.*, J. Synchrotron Radiat. **21**, 529 (2014).
25. F. Tian, X. H. Li, Y. Z. Wang, *et al.*, Nucl. Sci. Technol. **26**, 030101 (2015).
26. B. R. Pauw, J. Phys.: Condens. Matter **25**, 383201 (2013).
27. W. Q. Hua, Y. Z. Wang, P. Zhou, *et al.*, Chin. Phys. C **41**, 048001 (2017).
28. T. Sibillano, L. De Caro, D. Altamura, *et al.*, Sci. Rep. **4**, 6985 (2014).
29. Z. Zhou, C. Li, X. Bi, *et al.*, npj Comput. Mater. **9**, 58 (2023).

Supplemental Document

Optics Letters

Virtual X-ray critical dimension metrology via Monte Carlo simulation: supplement

JIAHAO ZHANG,[1,†] ZHANGYONG LIU,[1,†] WEIGANG ZHOU,[1] DINGXUAN DENG,[1] XIUGUO CHEN,[1,2,*] AND SHIYUAN LIU[1,2]

[1] *State Key Laboratory of Intelligent Manufacturing Equipment and Technology, Huazhong University of Science and Technology, Wuhan 430074, China*
[2] *Optics Valley Laboratory, Wuhan 430074, China*
[†] *These authors contributed equally to this work.*
[*] *xiuguochen@hust.edu.cn*

Supplement DOI: https://doi.org/10.6084/m9.figshare.27276282

Parent Article DOI: https://doi.org/10.1364/OL.536611

Virtual X-ray critical dimension metrology via Monte Carlo simulation: supplemental document

1. Detailed description of MC-VXCD method

At the exit plane of the Montel mirror (EM plane), the beam is described as a collection of photons, each defined by its position (x_0, y_0), direction (D_x, D_y), and energy (E). As shown in Fig. S1, these photons propagate the collimation system, interact with the nanostructure, and are subsequently collected by the detector. The subsequent sections detail these processes.

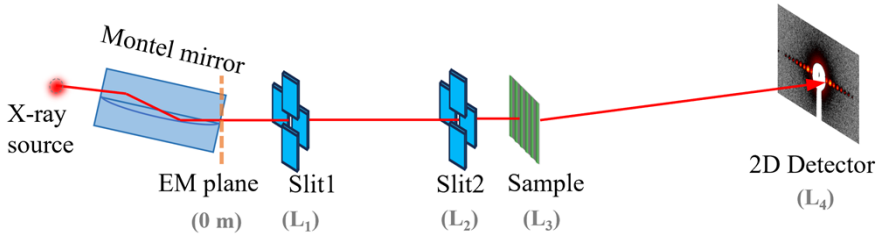

Fig. S1 Schematic of the basic system layout for XCD instrument.

1.1 Collimation System

The collimation system comprises two slits, each made up of four edges, positioned at distances L_1 and L_2 from the EM plane, respectively. The photon positions as they propagate to the two slits are determined by

$$\begin{cases} (x_1, y_1) = (x_0, y_0) + L_1 \cdot (D_x, D_y) \\ (x_2, y_2) = (x_0, y_0) + L_2 \cdot (D_x, D_y) \end{cases}. \tag{S1}$$

Photons within the slit aperture pass through the collimation system, while those outside this aperture are absorbed and do not interact with the sample.

1.2 Scattering of Nanostructures

Photons travel to the sample through the collimation system, with the distance between the sample and the EM plane denoted as L_3. Their positions are determined by

$$(x_3, y_3) = (x_0, y_0) + L_3 \cdot (D_x, D_y). \tag{S2}$$

Photons either penetrate the substrate or are absorbed, with a portion of the transmitted photons undergoing further elastic scattering with the nanostructures. The scattering cumulative distribution function (SCDF) and the photon scattering rate (SR) of nanostructures can be determined either through theoretical model calculation or by referencing experimental data from small-angle scattering beamlines at synchrotron radiation facilities. The subsequent sections provide a detailed description of both methods.

1.2.1 Theoretical model calculation

When photons interact with nanostructures at an incident angle ω, the intensity of scattering order of the nanostructure can be described by the following equation.

$$I(\boldsymbol{q}) = I_0 T_R N_p \left(\frac{r_e}{SDD}\right)^2 (\rho_e)^2 \left|F(\boldsymbol{q})\right|^2 S(\boldsymbol{q}) \mathrm{e}^{-q^2\sigma_{\mathrm{DWF}}^2} + I_{\mathrm{bkg}}, \tag{S3}$$

where $\boldsymbol{q}$ represents the scattering vector with magnitude of $|\boldsymbol{q}| = 4\pi \sin\theta/\lambda$. Its components along the X and Z directions are $q_x = |\boldsymbol{q}|\cos(\omega+\theta)$ and $q_z = |\boldsymbol{q}|\sin(\omega+\theta)$, respectively. I_0 denotes the incident photon flux, T_R is the transmittance of the sample, N_p represents the number of scatterers, r_e is the Thomson electron radius, $r_e = 2.818\times10^{-13}$ cm, SDD is the sample-to-detector distance, ρ_e is the electron density of the material, and $F(\boldsymbol{q})$ is the form factor, which is the Fourier transform of the sample's electron density distribution. $S(\boldsymbol{q})$ is the structure factor, described as $S(\boldsymbol{q}) = \delta\left(q_x - m\times\frac{2\pi}{pitch}\right)$. σ_{DWF} represents the Debye-Waller factor accounting for surface roughness, and I_{bkg} is the background scattering.

After calculating the intensity I_{m} of m-th diffraction order, the photon scattering rate is $SR = \sum_m I_m \Big/ I_0$, and the scattering cumulative density function is $SCDF(m) = \sum_{i=1}^{m} I_i \Big/ \sum_m I_m$.

1.2.2 Referencing experimental data from small-angle scattering beamlines

When using experimental data from a small-angle scattering beamline at a synchrotron radiation source as a reference, both the intensity of each diffraction order and the flux of the incident beam can be directly obtained, simplifying the calculation process for the scattering rate SR and the scattering cumulative density function SCDF. Using a one-dimensional nanostructure as an example, the one-dimensional scattering curve measured at normal incidence on the X-ray scattering beamline of Shanghai Synchrotron Radiation Facility are presented in Figs. S2(a). The sample's transmittance at 10 keV is 1.56%, and the photon scattering rate is 4.087×10^{-5}. When the scattering order exceeds the seventh order, the scattering signal becomes extremely weak. Therefore, only scattering from the –7th to the +7th order is considered, and the scattering cumulative distribution function (SCDF) is illustrated in Fig. S2(b).

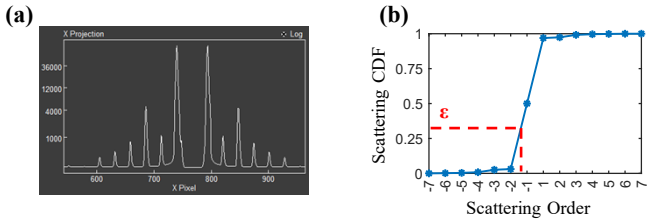

Fig. S2 Measurement results of one-dimensional nanostructures at normal incidence on the X-ray scattering beamline of SSRF: (a) one-dimensional scattering curve. (b) Scattering cumulative distribution function (SCDF) derived from the integrated intensity of each diffraction peak.

For photons reaching the sample, the number of scattered photons is initially calculated based on the transmittance of the nanostructure (67.9% at 24.1 keV) and the scattering rate. As shown in Fig. S2(b), a uniformly distributed random number ε within the range [0, 1] is generated for each photon, and its corresponding interval [$SCDF_{m-1}$, $SCDF_m$] is determined. The scattering angle 2θ of the photon can be calculated using Eq. (1) in the manuscript. Assuming the nanostructure period is oriented along the horizontal direction, the initial position of photons scattered by the sample becomes (x_3, y_3), with a propagation direction of (D_x + 2θ, D_y).

1.3 Scattering pattern acquisition of the detector

When scattered photons propagate to the detection plane, located at a relative distance L_4 from the EM plane, their positions are determined by

$$\left(x_4, y_4\right) = \left(x_3, y_3\right) + \left(L_4 - L_3\right) \cdot \left(D_x + 2\theta, D_y\right). \tag{S4}$$

The two-dimensional position sensitive detector records photons in the corresponding pixels. Assuming the relative distance between the ideal optical axis and the center of the detection plane is (dx, dy), and the pixel size is p, the index (M, N) of the pixel that records the photon is determined by

$$\left(M, N\right) = \left\lceil \left(x_4 - dx/p, y_4 - dy/p\right) \right\rceil, \tag{S5}$$

where $\lceil \bullet \rceil$ denotes the ceiling function. Applying the above calculations to all photons yields the scattering pattern recorded by the detector. For the selected photon-counting detector, its high dynamic range and absence of dark current noise reduce detector-induced errors. Information regarding the detector's quantum efficiency, non-linear response, and flat-field correction is included in the detector's documentation and forms an integral part of the virtual instrument. It is noteworthy that a beamstop is typically placed in front of the detection plane to block the excessively intense primary beam and prevent detector damage. Assuming the beamstop has a diameter D, photons within this range cannot be recorded by the detector, and the corresponding pixel intensity is set to zero.

2. Results of the calibration process

The virtual instrument functions as the digital twin of the actual instrument. To enable the virtual instrument to serve as an effective substitute, it must be configured with precise system parameters that align with the actual instruments.

The system calibration procedure involves two steps. The first step entails adjusting the distance between the detector and the EM plane with the slit fully open to fit intensity distribution and divergence of the beam. The distances were adjusted to 7250 mm, 6450 mm, 5250 mm, 4050 mm, and 2750 mm, respectively. Figures S3(a1) to S3(a5) display the primary beam images at each position. In fitting the primary beam intensity distribution, the photon position and divergence at the EM plane are described by a Gaussian distribution. Due to the asymmetry of the horizontal beam intensity distribution, a skewed Gaussian distribution is employed. Figures S3(b) and S3(c) present the fitting results of the primary beam intensity along the vertical and horizontal directions at the specified positions.

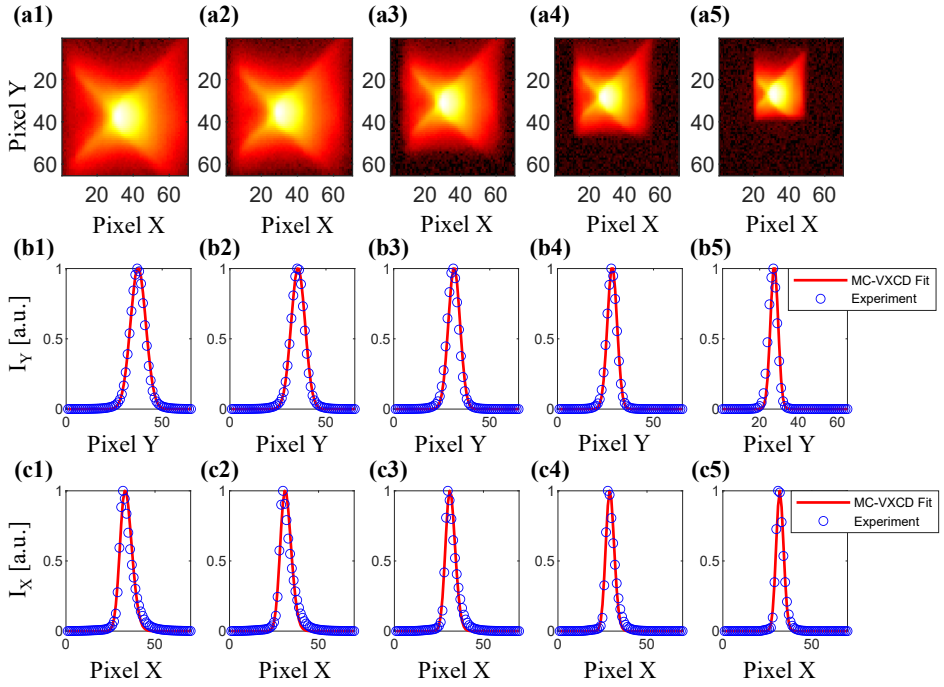

Fig. S3 Measurement and fitting results of the first step of system calibration. (a1) - (a5) The primary beam images when the distance between the detector and the EM plane is set to 7250 mm, 6450 mm, 5250 mm, 4050 mm, and 2750 mm, respectively. (b1) - (b5) The vertical intensity distribution fitted using MC-VXCD. (c1) - (c5) The horizontal intensity distribution fitted using MC-VXCD.

The second step involves calibrating the positions of the slits relative to the beam center. The distance between Slit 1 and EM plane is 230 mm, and the distance between Slit 2 and EM plane is 1830 mm. Each slit edge is sequentially adjusted until complete extinction is achieved to obtain the primary beam flux curve relative to the edge positions, which is subsequently fitted using MC-VXCD. As shown in Fig. S4, the positions of the two slits are calibrated in MC-VXCD, which ensures finer adjustment and optimization of the collimation system configuration. Errors introduced by experimental adjustment cause deviations in the actual

beam distribution from the ideal Gaussian profile, resulting in discrepancies in the relative intensity curve, as shown in Fig. S4. This can be addressed with improved consistency by incorporating additional parameters to more accurately characterize the scattering intensity distribution.

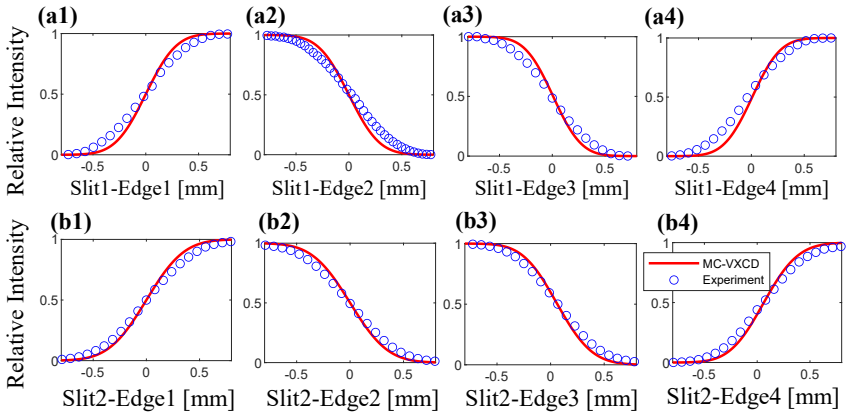

Fig. S4 Measurement and fitting results of the second step of system calibration. (a1) - (a4) Variations in primary beam flux and the MC-VXCD fitting results as the four slit edges of Slit 1 are adjusted. (b1) - (b4): Variations in primary beam flux and the MC-VXCD fitting results as the four slit edges of Slit 2 are adjusted.

3. Effect of exposure time variations on scattering signal error

Exposure time influences the signal-to-noise ratio of the scattering signal. Utilizing our home-built instrument, the time-normalized 9000 s scattering curve was designated as the ground truth (GT). Exposure times were then reduced to 3600 s, 1800 s, 1200 s, and 600 s. The time-normalized scattering curve is calculated as

$$I_N(T,q) = \frac{I(T,q)}{T}, \tag{S6}$$

where $I(T,q)$ is the integrated scattering curve at exposure time T. The formula for calculating relative error is

$$\text{Rel-Error} = \frac{I_N(T,q) - I_{GT}}{I_{GT}}, \tag{S7}$$

The relative errors of the time-normalized scattering curves, in comparison to the GT, are presented in Fig. S5. As exposure time decreases, the oscillation amplitude of the relative error curve increases markedly, with larger errors occurring in regions of lower theoretical scattering intensity, such as at higher scattering vectors and between scattering peaks. This suggests that the scattering process is limited by Poisson noise.

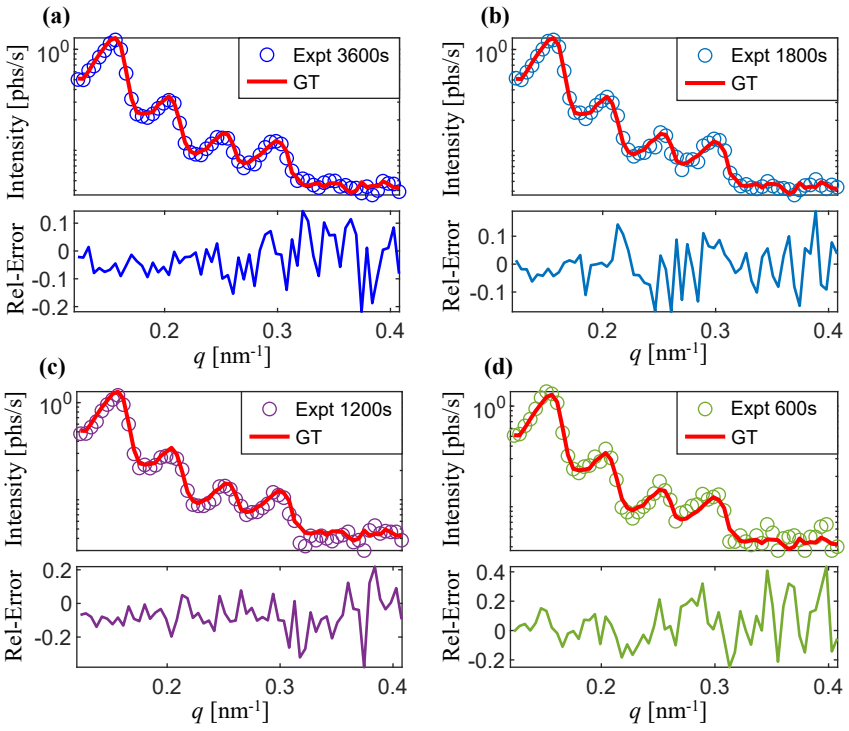

Fig. S5 Time-normalized scattering curve and relative error to GT with reducing exposure time.